DOI:10.53539/squjs.vol29iss3pp59-78

Sultan Qaboos University Journal for Science

Journal page: www.squ.edu.om/index.php/squjs/index

Photoluminescence and Dye Adsorption Mechanism of Dehydrated Carbon Quantum Dots

Basim Al Farsi[1*], Hamood Al Shidhani[1] , R.G. Sumesh Sofin[1*], El-Said I. El-Shafey[2], Zainab B. Al-Ruqeishi[2], Abdullah S. Al-Hosni[3], Abey Issac[1], Abdulrahman Al Nabhani[4] , Mohamed Al-Kindi[4] and Osama K. Abou-Zied [2]

[1]Department of Physics, College of Science, Sultan Qaboos University, PO Box 36, Al Khoud, Muscat, PC 123, Oman; [2]Department of Chemistry, College of Science, Sultan Qaboos University PO Box 36, Al Khod, Muscat, PC 123, Oman; [3]Diwan of Royal Court, Oman Botanic Garden, PO Box 808, Al Khoud, Muscat, Oman; [4]Department of Biomedical Science, Pathology, College of Medicine & Health Sciences, Sultan Qaboos University, PO Box 36, Al Khoud, Muscat, PC 123, Oman.

*Email address: basem.alfarsi@gmail.com (Basim Al Farsi); sofins@squ.edu.om (Sumesh Sofin)

ARTICLE HISTORY

Received 29 February 2024
Received revised 27 April 2024
Accepted 3 June 2024

ABSTRACT: The role of oxygen-based functional groups in the photoluminescence of dehydrated carbon dots (DCs) and the adsorption mechanism of dye molecules onto the surface of DC is investigated. DC were prepared from orange peel for the first time via the chemical dehydration effect of sulfuric and phosphoric acid at 180 ºC. We compared the emission spectra of DCs in different solvents in great detail. The solvatochromism of DC in different solvents is discussed. The role of oxygen-based functional groups in the light emission process is examined. Adsorption of methylene blue (MB) on the surface of DC was studied at different contact times, pH, concentrations, and temperatures. In this work, we used Langmuir and Freundlich adsorption models for the analysis. Sorption kinetic data were found to fit well with the pseudo-second-order model. Our results also showed increased MB adsorption capability with temperature. The results are essential for the application of CQDs, such as in wastewater treatment.

Keywords: Photoluminescence; Adsorption; Solvatochromism; Carbon dots; Methylene blue (MB).

آلية الانبعاث الضوئي وامتزاز الصبغة للكربون النقطي الكمي منزوع الماء

باسم الفارسي، حمود الشيذاني، ر.ج. سوميش صوفين، السعيد إبراهيم الشافعي ، زينب بدر الرقيشي ,عبد الله سعيد الحوسني، أبي إسحاق ، عبد الرحمن النبهاني ، محمد الكندي وأسامة كمال أبو زيد

الملخص: تم دراسة دور المجموعات الوظيفية المعتمدة على الأكسجين في الأنبعاث الضوئي للكربون الكمي منزوع الماء (DC) وآلية امتزاز جزيئات الصبغة على سطح الكربون الكمي منزوع الماء (DC). في البداية تم تحضير الكربون الكمي منزوع الماء (DC) من قشر البرتقال عن طريق تأثير الجفاف الكيميائي لحمض الكبريتيك والفوسفوريك عند 180 درجة مئوية. قارنا أطياف الانبعاث للكربون الكمي منزوع الماء (DC) في مذيبات مختلفة بالتفصيل. نوقشت المذيبات اللونية للكربون الكمي منزوع الماء في المذيبات المختلفة. حيث فحص دور المجموعات الوظيفية المعتمدة على الأكسجين في عملية انبعاث الضوء. وتم دراسة امتزاز أزرق الميثيلين (MB) على سطح الكربون الكمي منزوع الماء (DC) في أوقات تلامس مختلفة ودرجة الحموضة والتركيزات ودرجات الحرارة. في هذا العمل، استخدمنا نماذج الامتزاز لانجمير وفريندليتش للتحليل. تم العثور على بيانات حركية الامتصاص تتلاءم بشكل جيد مع نموذج الدرجة الثانية. حيث أظهرت نتائجنا أيضا زيادة في قدرة امتصاص MB مع درجة الحرارة. تعتبر النتائج حاسمة في تطبيقات الكربون الكمي، مثل معالجة مياه الصرف الصحي.

الكلمات المفتاحية: اللمعان الضوئي، الامتزاز، المذيبات اللونية، الكربون النقطي ، أزرق الميثيلين (MB)

1. Introduction

Organic dyes are widely employed in various industries, such as printing, cosmetics, shoe polish, textiles, paper, leather, and dishwashing liquids [1, 2]. During the coloring process, enterprises generate large amounts of wastewater containing complex dyes, causing significant environmental issues that threaten the survival of living species [3]. As a result, a lot of effort is needed to develop efficient processes for removing color dyes from wastewater [4]. Because of its structure and strong chemical bonding properties, methylene blue (MB, $C_{16}H1_8CIN_3S$), a stable cationic dye, is challenging to decolorize [5]. However, despite the fact that MB is extremely harmful to all kinds of life, it is still commonly used in the dyeing industry [1, 6]. Various physical and chemical mechanisms, including adsorption, oxidation, ion exchange, and filtration, have been used to eliminate dye molecules from sewage water [7-9]. The oxidation procedure is not energy efficient and yields toxic substances. Adsorbent regeneration is a big problem in the ion exchange process. The molecular adsorption method provides a cost-effective, and efficient technique due to its simplicity of design and operational adaptability [1, 10].

Recently, many researchers have focused on the applications [11, 12] of functionalized carbon-based materials in wastewater treatment [13], biomedical treatments/ imaging [14], energy storage [15], catalysis, and sensing [16]. The impetus for the choice of this material is aroused due to the ionic and aqueous stability, striking optical properties (visible emission spectrum, excited-state lifetime of a few nanoseconds), pH sensitivity, non-toxicity, low production cost, biocompatibility, and ease of functionalization [17-19].

Various organic materials, including activated carbon (AC), dehydrated carbon (DC), carbon nanotubes, and graphene, have been employed as adsorbents. Alaor et al., for instance, used a chemical activation process to produce AC from plant sludge, which was then deployed to remove cationic dyes from wastewater. They found a maximum capability of about 96 % for the removal of specific organic dyes [20]. Kuang et al. showed that surface-modified AC significantly improved the adsorption of organic dyes [11]. They found many factors that significantly affect the adsorption properties, such as initial dye concentration, temperature, pH of the initial solution, contact angle, adsorbent dosage, and the presence of salts [11]. They also have synthesized DC from date palm leaflets using concentrated sulfuric acid [12]. They reported that the prepared DC had a low surface area and a large adsorption capacity that facilitated fast adsorption of MB [12].

However, the effect of temperature on the adsorption mechanism is not found in their study. DC has a low pHzpc with a large number of acidic functional groups (lactonic, carboxylic, and phenolic) [12]. The researchers synthesized oxidised activated carbon (OAC) with an acidic surface by a chemical activation process of date palm leaves using potassium hydroxide (KOH), followed by nitric acid oxidation. The results showed that the OAC possesses a lower surface area than AC. Further, Langmuir model fits equilibrium adsorption data for hydrophobic activated carbons (HAC-EA) with the highest MB adsorption capacity compared to the Freundlich model. Most likely, the dominant adsorption forces acting on MB by different types of carbon surfaces are hydrophobic forces of hydrophobic activated carbons (HACs), hydrogen bonding in the case of basic activated carbons (BACs), electrostatic force of OACs, and van der Waals forces of ACs [8]. It should be mentioned here that the synthesis of AC is expensive as it involves high energy-consuming preparation steps and oxidation steps to place carboxylic groups on the dots prior to surface functionalization [8, 21]. In contrast, the synthesis of DC is cheap and, because of its high carboxylic content, can be functionalized directly via amide coupling [12]. Another important aspect of CQDs is that they are fluorescent [19, 22, 23]. However, the photoluminescence (PL) mechanism is still not clear and is largely attributed to the functional groups on the surface of the particles. To the best of our knowledge, the PL characteristics of dehydrated carbon dots are not well studied.

DC can be synthesized by mixing a base material with phosphoric acid (DCP) or sulfuric acid (DCS) at low temperatures. When water and other volatile materials are lost, the feed material decomposes during carbonization with dehydration [12, 24]. Several reports are available regarding the usage of different types of green wastes in the synthesis of DC, such as Cocoa Pod Husk [25], pomelo peal [24], egg-yolk oil [26], ascorbic acid [23], orange juice [27], as well as date palm leaflets [8]. Herein, DC dots are prepared via the dehydrative effect of H_3PO_4 or H_2SO_4 on the agricultural green waste of mandarin peels as the base material. A number of characterization tools were used to determine the structure and morphology of DC, as well as the surface concentrations of the different functional groups. We examined the PL properties of DCP and DCS to better understand the light emission mechanism. The solvatochromism of DCP-DCS in several solvents, including water, methanol, ethanol, and acetone, is also explored. The surface adsorption mechanism of MB on DC samples is also studied in terms of mass ratio, pH, kinetics, and equilibrium at two different temperatures 20 ^{o}C and 40 ^{o}C.

2. Experimental

2.1. Materials

All chemicals used in this study are of analytical grade and were utilized in their original form, without further purification. Mandarin peels were sun-dried and washed several times with deionized water to remove surface contaminants. This was followed by a second round of drying at ambient temperature. Small pieces (1-2 cm) of clean and dry Mandarin peels were then used to synthesize carbon dots.

2.2 Preparation of dehydrated carbon dots (DCS-DCP)

Two types of dehydrated carbon dots (DCS and DCP) were synthesized by treating dry and clean Mandarin peels (20 g) with dilute acids (3.4 molar concentration) such as H_2SO_4 (to prepare DCS) and H_3PO_4 (to prepare for DCP). The samples were carbonized between 8 and 12 hours at 180 ^oC in an oven (Hobersal Mon XB2-125 furnace, Hobersal, Spain). Next, the black product was washed in a Buchner funnel with warm deionized water until the filtrate became acid-free (until no color change was detected with methyl orange). The samples were then oven-dried for 24 hours at 105^oC. The DC samples were then stored in a clean, well-closed polyethylene bottle containing nitrogen gas. Figure 1 outlines the preparation routes of DCS and DCP samples.

2.3 Sample characterization

The crystal structure and morphology of CQDs were investigated using an X-ray diffractometer (XRD) (Philips diffractometer, model PW 1820; with a Cu- K source; wavelength = 1.540 Å.) and a Transmission Electron microscope (TEM, model JEM-1500-JEEM) and a Transmission Electron microscope (TEM, model JEM-1400-JEOL). The surface microstructure was determined using a field emission electron microscope (FESEM; Jeol JSM-7800F). Elemental characterization of the samples was carried out by using Energy-dispersive X-ray spectroscopy (EDX, model Jeol JSM 5600, Japan), X-ray photoelectron spectroscopy (XPS, Omicron Nanotechnology, Germany with Al-Kα radiation operating at 15 Kv) and a CHNS/O analyzer (Euro EA 3000 elemental analyzer, UK). Casa XPS software (Casa Software Ltd, UK) was used to examine the XPS results. Functional groups on the CQD surface were identified by Fourier transform infrared (FT-IR) absorption spectroscopy (FT-IR spectrometer, PerkinElmer, Spectrum One, USA, within the range 4000 – 400 cm^{-1}; at a scan resolution of 4 cm^{-1} in 40 scans). Compact pellets prepared from the mixture of 0.005 g of carbon dots and 0.995 g of KBr were used for the FT-IR measurements. Boehm titration with selective base neutralization capacity was used for the quantification of functional groups such as carboxyl, lactone, phenol, and carbonyl on the sample surface [28]. DCP or DCS (0.125 g each) was added to 25 ml standard solutions of 0.1 M NaOH, 0.05 M Na_2CO_3, 0.1 M $NaHCO_3$, and 0.1 M NaOEt in decarbonated water. The mix was prepared in 30 mL polyethylene vials. To avoid the possibility of carbon auto-oxidation (due to base-catalyzed auto-oxidation) each sample was flushed with N_2 for 5 minutes to eliminate oxygen [29]. The samples were then placed in a shaking water bath at 25 °C and 200 rpm for 48 hours in order to reach equilibrium. All aliquots were titrated against a standard 0.1 M HCl solution with methyl orange to determine the concentration change of each solution. Zeta potential measurements at different solution pH were measured using the SurPASSTM electrokinetic analyzer (UK). The pH was adjusted with 0.01 M HCl and NaOH during the experiment. The method reported by Moreno-Castilla et al. was employed to calculate the Zero-point of charge (ZPC) (see SI (a)). [30] [13, 31, 32]. The surface area of DC was calculated from the nitrogen adsorption values at 77 K using the ASAP 2020 instrument (Micro metrics, USA). The samples were degassed for 8 hours at 70 °C under vacuum to avoid any changes on the surface at higher temperatures [8]. UV-Visible absorption spectroscopy was done utilizing Agilent 8453. PL spectroscopy was carried out using Shimadzu RF–5301 spectrometer. The excitation wavelength used is 350 nm, where we observed the maximum emission intensity. A fluorescence emission lifetime spectrometer was used for the time-resolved measurements (TimeMaster, Photon Technology International). The authors used a 310 nm pulsed LED (pulse width of 9×10^{-4} ns) with two long-pass filters (295 nm and 320 nm) and a.

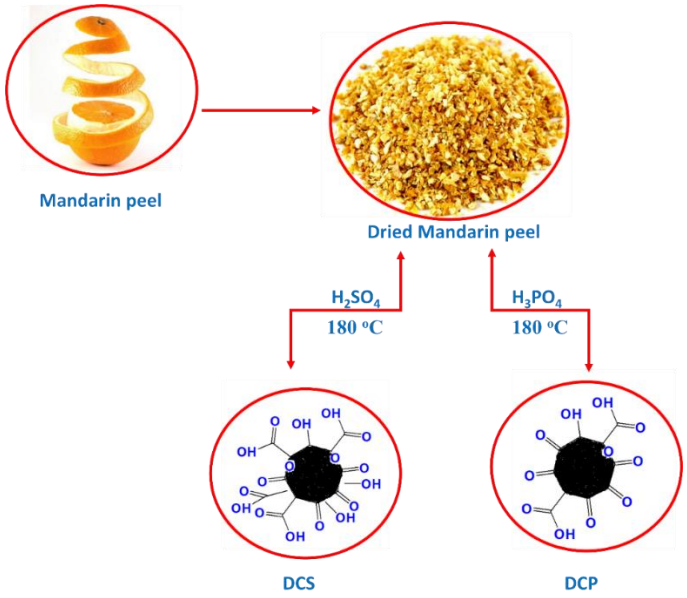

Figure 1. Preparation routes of DCS and DCP samples.

2.4 Adsorption studies of Methylene blue (MB)

Methylene blue was diluted into a 1000 mg/L stock solution in deionized water (DIW). A standard or reference solution and solutions at various concentration levels of MB were prepared from the stock solution. To study the effect of pH, 0.06 g of dots (DCS or DCP) were added to 25 mL of MB solutions (concentration:100 mg/L) having various initial pH values (2-10) at 20 °C. The pH values of MB solutions were adjusted by adding drops of dilute HCl or NaOH solution before mixing the dots. The samples were agitated for 48 hours to achieve equilibrium. Aliquots of supernatants were then analyzed using a Varian/Cary/50 Conc UV–vis spectrophotometer. Keeping DIW as the reference, the residual MB was detected spectrophotometrically at λ_{max} 665 nm. The samples for the kinetic experiments had 0.12 g of dots in 50 mL MB (concetration:100 mg/L) solution in DIW. Before reaching the equilibrium, aliquots of supernatant were analyzed at various intervals. The samples for the equilibrium studies had 0.06 g of dots in 25 mL of MB solutions in DIW, having different concentrations of MB (100–500 mg/L). Until equilibrium was reached, the samples were mechanically stirred at a rate of 100 rpm/min. The kinetic and equilibrium measurements were done at an initial pH of 7 and at two temperatures (20 and 40 °C). In order to study the role of dot concentration on MB adsorption, different amounts of dots (0.03-0.12 g) were added to 25 mL of MB solutions (100 ppm) at 20 °C. The solutions were then agitated until equilibrium was reached. A part of the adsorption solution was taken for analysis to determine the MB content. All measurements were repeated at least two times.

3. Results and Discussion

3.1 Structure and morphology of DCS

Figure 2 shows the X-ray diffraction patterns of the carbon dots. The broad asymmetric peaks at 2θ ~23.8° and ~43.1°can be attributed to (002) plane of graphite lattice, respectively (JCPDS File, No. 1-640) [33-36]. The XRD results are similar to previous reports[13, 19, 33, 37]. The broadness of the peaks could be due to poor graphitization [33]. The TEM images (see representative images shown in Figure 3a and b) show the average particle size of DCP to be 3.34±0.1nm (see Figure 3(c)). In contrast, the average particle size of DCS is 2.63±0.2 nm, as shown in Figure 3(c). The difference in the particle size may be due to the difference in the surface etching rate of the dots during the acid treatments [19, 38]. The average lattice spacing is found to be 0.29±0.01 nm for DCP and 0.27±0.01nm for DCS, which are again close to the spacing of (002) planes of graphite (0.34 nm) (see Figure 3(e-f))[39].

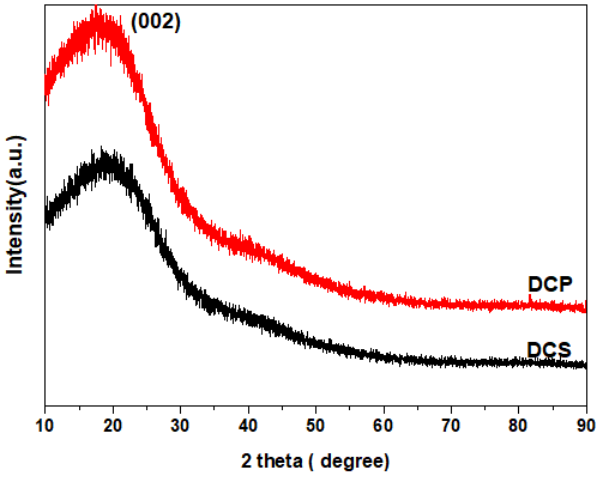

Figure 2. X-Ray Diffraction scans of DCP and DCS samples.

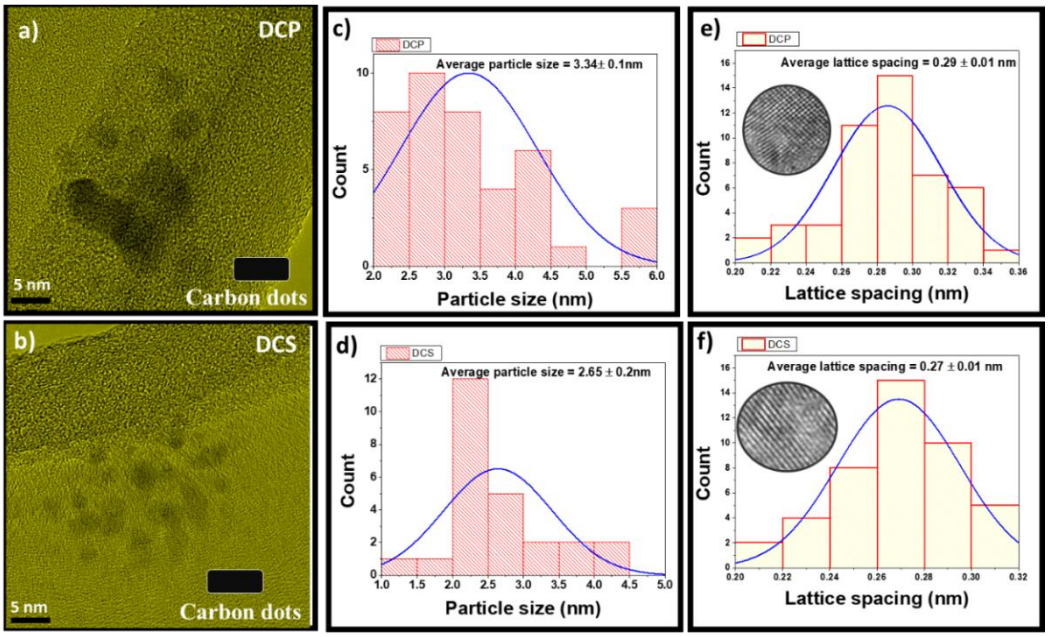

Figure 3(a-d). TEM images of **(a)** DCP, **(b)** DCS, the distribution of the particle size **(c–d)**, and **(e–f)** the lattice spacing of DCP and DCS, respectively.

3.2 Surface chemical properties

FTIR spectra (see Figure 4.a) show well-defined broadband near 3450 cm^{-1} (˙OH stretching vibration) attributed to the wet chemical treatment of the dry orange peels. DCS and DCP have bands at 1034, 1199, 1618, 1725, and 2918 $cm^{-1,}$ which can be attributed to C-O bending, C=C, carboxylic group (C = O), and C-H stretching vibrations in the CH_3/CH_2 groups respectively [40-42]. DCS prepared by the sulfuric acid treatment generally has more carboxylic groups than DCP which is prepared using phosphoric acid. The point of zero charges (pHzpc) of DCP and DCS are 4.80 and 4.24, respectively. This indicates higher surface acidity for DCS than DCP. This could be due to more proton-donating groups, such as –COOH on DCS, than on DCP [43]. It can also be related to sulfuric acid's higher oxidation power than phosphoric acid during the treatment [43, 44]. Figure 4c shows the change in zeta potential (δ) of the dots with the solution pH. The value of δ decreases significantly when pH increases. Both samples show a crossover from positive to negative values of δ with increasing pH. The data was fitting using the Boltzmann equation [45].The pH at which δ=0 is around 3.62 ± 0.6 for DCP and 3.26 ± 0.4 for DCS (see Fig 4c). The negative surface charge is due to hydroxyl ions (OH-) on the dot surface [46]. A study by Harry et al. shows that deprotonation of carboxyl groups can occur in the pH range between 2 to 6 [47]. The results indicate a higher amount of the carboxylic group on DCS than on DCP.

The amount of carboxyl, lactone, carbonyl, and phenol functional groups on the dots was measured using selective neutralization capability and was carried out using the Boehm titration method [28]. The surface functionality (meq/g) of DCS and DCP is shown in Figure 4d. The results indicate that DCS has higher carboxyl, lactone, and phenol functional groups than DCP. Moreover, it is noticeable that the percentage of the carbonyl group density is around 1.18 meq/g in the DCP sample compared to DCS, which is about 0.52 meq/g. In contrast, the carboxylic group density in the DCP and DCS samples are 0.94 and 3.14 meq/g, respectively.

3.3 EDS and CHN or CNHS/O

CHN and EDS data for DCS and DCP samples are displayed in Figure 5 and Table 1, respectively. The oxygen content is expressed as the percentage difference [100%−(C%+H%+N %)] [48]. The percentage of oxygen is higher in DCS, compared to DCP. The O/C ratio is found to be 0.55 in DCP and 1.07 in DCS (51.4% higher). At the same time, the H/C ratio is also 78.4% higher in DCS (0.097) compared to DCP (0.076). The higher H/C ratio in the case of DCS could be due to the increase in the amount of CH_3 group, while the rise in the O/C ratio could be because of the increased CO_2 carboxylation [49].

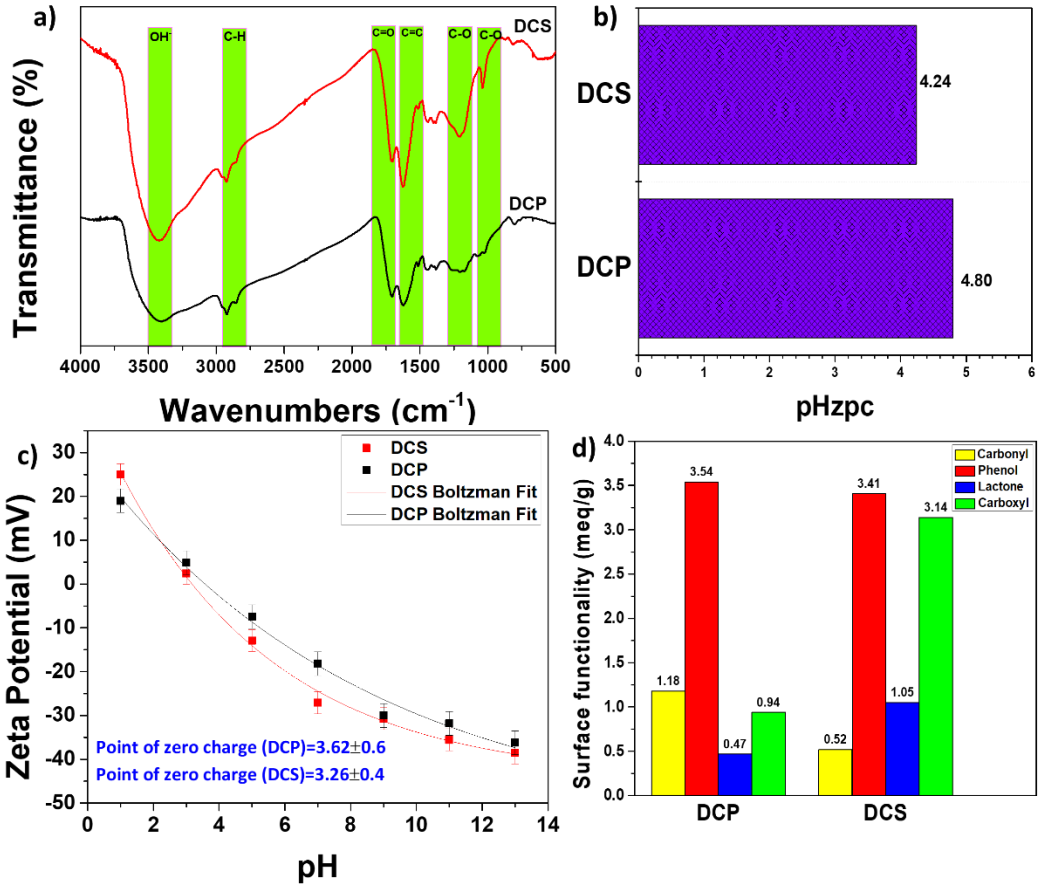

Figure 4. (a) FTIR spectra, (b) pHzpc, (c) change in zeta potential with pH and (d) the surface functionality of DCP and DCS samples.

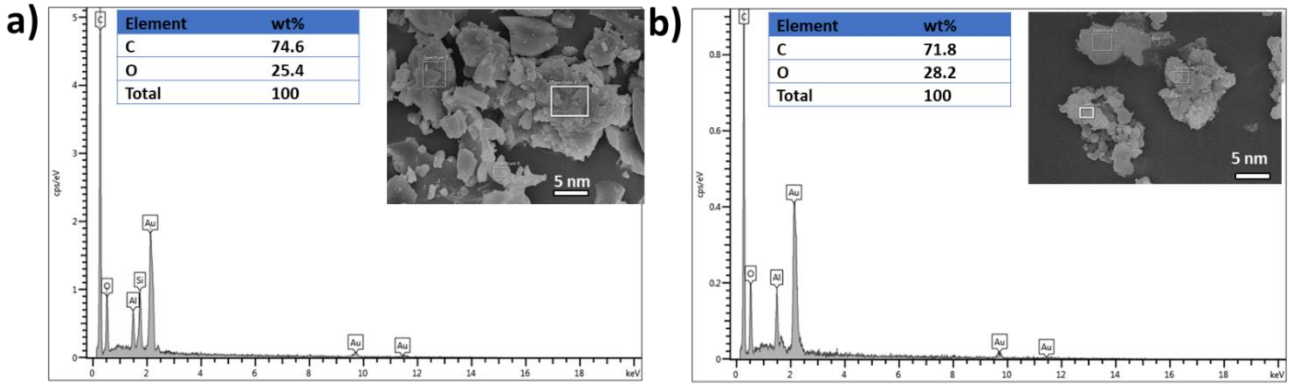

Figure 5. SEM micrographs of (a-b) dehydrated carbon (DCP and DCS, respectively).

Table 1. Results of EDS and CHN studies of DCP and DCS.

Elemental analysis	Element	Weight (%)	
		DCP	DCS
EDS	C	74.6	71.8
	O	25.4	28.2
CHN	C	61.6	46.01
	H	4.7	4.44
	N	-	-
	O	33.7	49.55
	H/C	0.076	0.097
	O/C	0.55	1.07

3.4 Thermal characterization (thermal analysis and chemical stability)

TGA and DSC results of DCP and DCS are shown in Figure 6 (a, b). The C-O groups on DCP and DCS form H-bonds with water molecules. In the range 16-200˚C, the decreasing weight percentage is because of water evaporation [12, 19]. The weight loss is 5.4% for DCP and 8.6% for DCS. The second region shows a steep weight loss of 31.06% for DCP, 34.39% for DCS in the temperature range from 200˚C to 375˚C, which could be related to a steady loss of oxygen-containing groups [19, 50, 51]. In the third region, between 375ºC and 800ºC the observed loss could be due to the dissociation of carbon bonds [51]. The weight loss of the DCP and DCS was about 48% and 53.1%, respectively. The DSC plots (see Figure 6b) indicate an endothermic process from 14°C to 221°C. The reason for this could be the loss of water molecules. The successive endothermic peak appears near 400°C, which could be due to the decomposition of carbon bonds. The DSC results agree with.

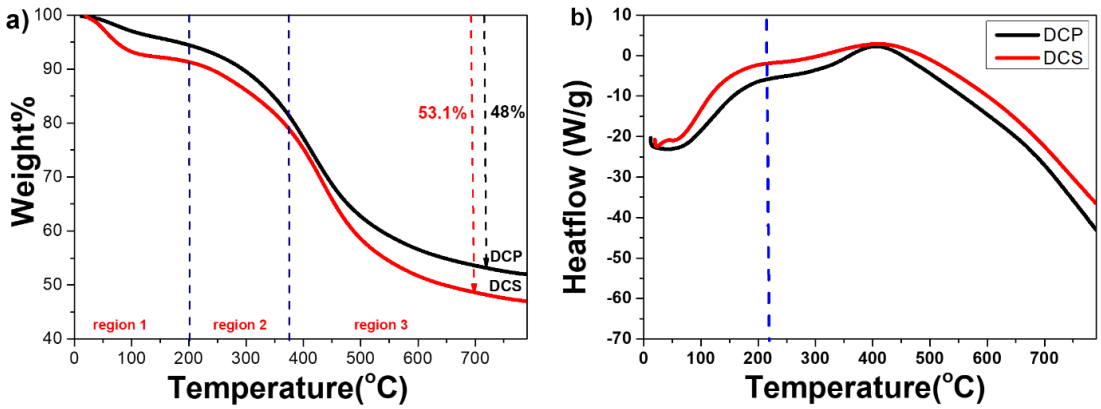

Figure 6. (a) TGA and (b) DSC of DC dots.

3.6 UV-Vis absorption studies

UV-Vis absorption spectra were measured on both DC samples dispersed in organic solvents such as ethanol, methanol, and acetone (see Figure 9(b-d)). The absorption observed at 223nm could be associated with the π- π* transition of aromatic C-C, C=C, bonds in π-conjugated sp^2 carbon core [53]. The second absorption peak observed at 327nm (methanol), and 340 nm (ethanol) can be attributed to n- π* transition of non-conjugated electron orbitals in carboxyl (C=O) bonds [53-56]. The absorption spectrum of DC in acetone is different from methanol and ethanol. Acetone is a typical Lewis acid; the other two solvents (methanol and ethanol) are Lewis bases [57]. Absorption studies suggest that the interaction between solvent molecules and the functional groups affects the electronic transition probability matrix.

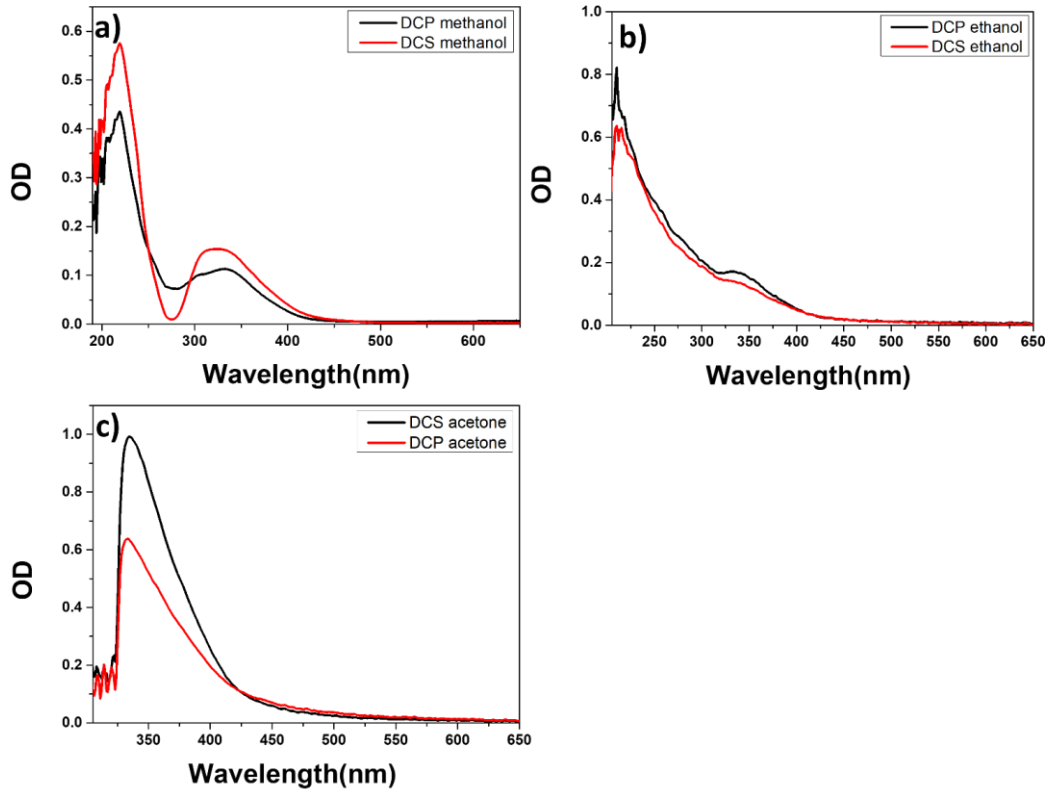

Figure 9. (a) UV Vis spectra of DCP-DCS in a) methanol solvent, **(b)** DCP-DCS in ethanol solvent and **(c)** DCP-DCS in acetone solvent.

3.7 Photoluminescence (PL) Analysis.

Emission spectra of DCP and DCS particles dissolved in methanol, ethanol, and acetone are displayed in Figure 11. a, b Solvent polarity has a vital role in the emission characteristics of fluorescent materials. Figure 11 a, b demonstrate that the PL peak exhibits a hypsochromic shift and the FWHM broadens with increasing solvent polarity (the increasing order of polarity is acetone, ethanol and methanol). The high polar solvent exhibits this broadening, possibly as a result of a prolonged nonradiative relaxing process [58]. In a highly polar solvent, a significant solvation effect can induce a redshift in emission. It is known that the energy gap of the fluorescent species decreases due to its interaction with polar molecules of the solvent,[23, 58]. In addition, the hydrogen bonds between polar protic solvents and the p-PD in carbon dots could result in charge transfer and conformational modifications. The deconvoluted (Multi-Guassian peak fits with $R^2 = 0.9999$) PL spectra show three sub-peaks in the case of DCS and DCP samples (see Figure 11 and Table 5). The sub-peaks are marked as Peak 1 (392 nm or 3.16 eV), Peak 2 (422 nm or 2.9 eV), and Peak 3 (498 nm or 2.49 eV). Origin of these peaks can be attributed to specific functional groups present on the surface of the dots from the following arguments.

The HOMO and LUMO energy gap for 20 aromatic rings, is calculated to be just 2 eV by Fang et al.[59, 60] . The authors claim that the PL emission from the carbon crystalline core for nanodots is minor. This is because, if we consider a 5nm core there would be roughly 500 aromatic rings with an energy gap smaller than 2 eV. However, some chances that isolated sp^2 clusters with a significant energy gap could be connected to the dot's surface, showing02 PL emission. The three deconvoluted peaks in the emission spectra of our samples should be arising from three separate processes. Isolated sp^2 clusters adhering to the dots could be the source of the largest energy peak (Peak 1). This is because the HOMO-LUMO energy gap of isolated sp^2 clusters' π-π^* levels was identical to that of pyridine derivative units (The energy gap is roughly 3 eV) coupled to the carbon core [19]. This energy gap is significantly higher than the energy of surface states. The carbonyl group has a HOMO-LUMO energy gap of approximately 2.5 eV. Consequently, Peak 3, which contributes the least to the total PL intensity, could be due to the surface carbonyl groups[19]. Carboxylic groups have PL emission at 2.9 eV and could be the origin of peak 2, representing the remaining fraction of the total emission [19]. The hypsochromic shift with increasing solvent polarity is mainly happening in Peak 3, which originates from the carbonyl group. The Carbonyl group is polar, and the interaction with solvent molecules can be more compared to other groups on the surface of the dots. The peak area is found to decrease with increasing polarity of the solvents. This could be due to increasing non-radiative transitions because of strong vibrational coupling with solvent molecules.

Table 5. Deconvoluted PL emission peaks of DCP and DCS in different solvents.

Sample Name		Peak position (±1 nm)	Intensity (a.u)	FWHM (nm)	Area (a.u)	Averaged Area%
Acetone						
DCP	**Peak c1**	392	73	50.00±0.03	5374.3± 0.7	19.4
	Peak c2	433	136	76.10±0.03	7318.2± 0.8	26.4
	Peak c3	498	91	160.70±0.02	15000.3± 0.8	54.2
DCS	**Peak c1**	392	1295	16.40±0.01	21646 ± 1	13.3
	Peak c2	433	1495	22.65±0.01	51534.1± 0.9	31.6
	Peak c3	498	754	93.58±0.01	90040 ±1	55.2
Ethanol						
DCP	**Peak c1**	391	35	53.70±0.01	1600±0.9	13.7
	Peak c2	433	55	70.00±0.01	3566.6±0.9	30.6
	Peak c3	482	49	142.60±0.02	6485.6±0.9	55.7
DCS	**Peak c1**	391	30	56.50±0.03	1326.9±0.8	11.7
	Peak c2	433	61	74.24±0.02	4659.5±0.6	41.0
	Peak c3	486	40	143.40±0.04	5385.2±0.7	47.4
Methanol						
DCP	**Peak c1**	392	63	13.0±0.1	1327.4±0.1	15.2
	Peak c2	433	93	58.40±0.08	2343.1±0.5	26.83
	Peak c3	475	115	96.99±0.02	5101.4±0.5	58.42
DCS	**Peak c1**	390	43	67.10±0.03	2512.2±0.7	14.74
	Peak c2	433	89	80.80±0.03	6991.8±0.8	41.01
	Peak c3	480	60	137.00±0.03	7542.9±0.9	44.24

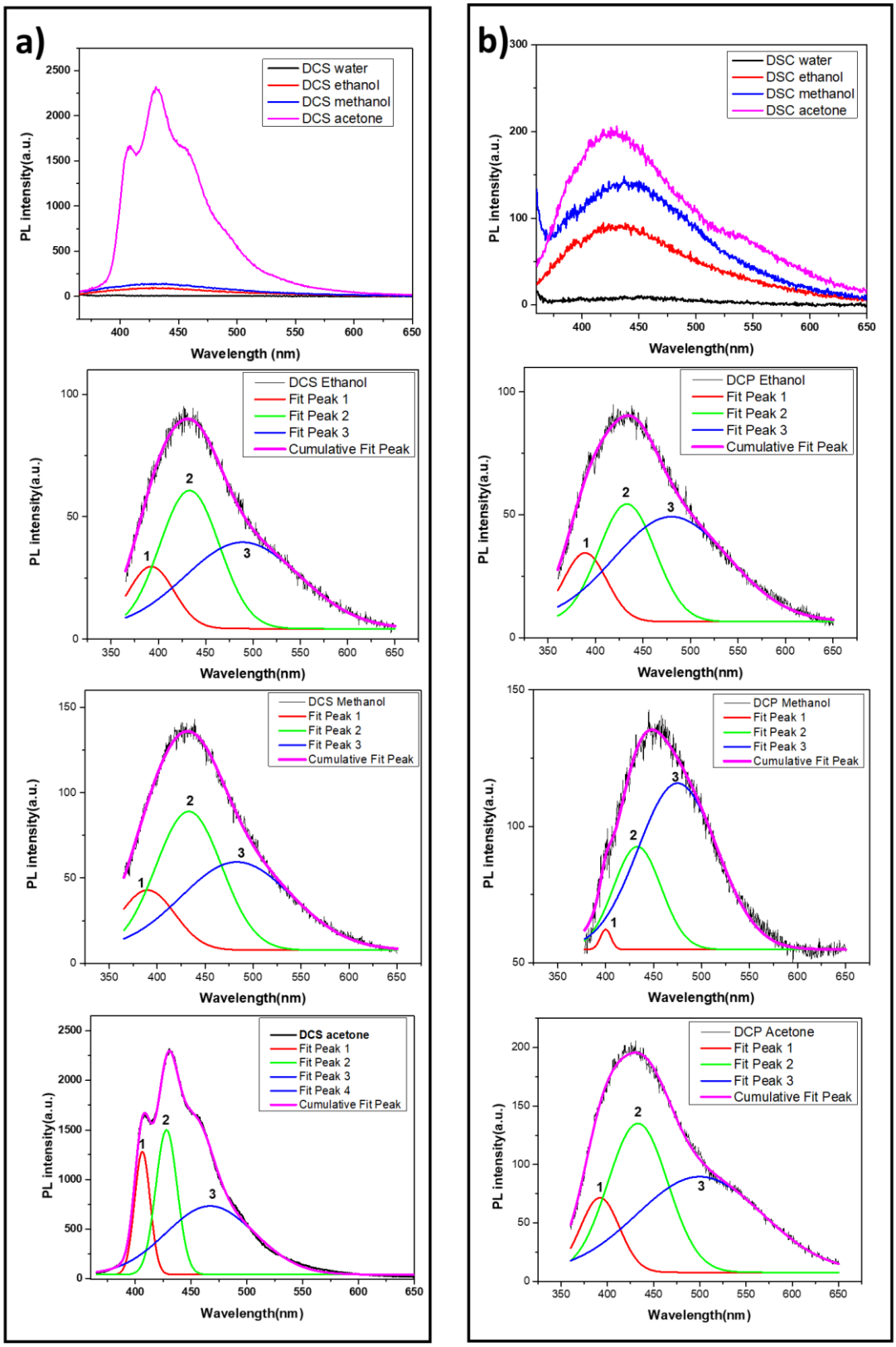

Figure 11. Room-temperature photoluminescence spectra for a) DCP and b) DCS in different solvents with de-convoluted emission peaks.

3.8 Time-Resolved Emission Spectroscopy

Figure 12 a, c shows the decay transients of DCP and DCS in various solvents. There are fast and slow components in the transients. Note that the average lifetime depends on the polarity of the solvent. It decreases when the polarity of the solvent increases. In high-polarity solvents such as methanol, the average lifetime is 1.4 ns (DCS) and 1.27 ns (DCP). Whereas, in acetone, the average lifetime is around 2.98 ns (DCS) and 2.27 ns (DCP), as shown in Figure 12 b, d. As discussed earlier, the vibrational energy level coupling of the functional group with the solvent group can lead to increasing non-radiative transitions. This could lead to reduced emission lifetime in polar solutions. The lifetime of DCS and DCP in acetone is longer than dots in methanol and ethanol, asserting the above discussion. Different solvents' interactions can influence their emission due to oxygen-containing functional groups, especially the carbonyl group on the surface of the dots [61].

3.9 Surface area and porosity

Figure 7 shows the nitrogen adsorption/desorption isotherms at 77 K. Both Type I and Type IV isotherm characteristics are identified according to the classification reported by Sing et al [62]. Compared to activated carbons, DCP and DCS show, in general, low surface area, which is typical for dehydrated carbon dots [12]. Both samples show H3 hysteresis loop types that at high values of relative pressures (P/Po), do not show limiting adsorption (Figure 7). This could be related to the aggregation of particles [62]. Total surface area (S_{BET}) was calculated by the Brunauer, Emmett, and Teller equation (BET, see eqn. (1)) [58]. $S_{micro} = S_{BET} - S_{meso} \quad eqn.$ (1). Where S_{BET}, $S_{meso,}$ and S_{micro} are total surface area, mesopore surface area, and micropore surface area, respectively. Vt, the total pore volume was calculated (based on the Gurvich rule) by using the nitrogen adsorption data at P/Po=0.98, [63]. The t-plot method [63] was used to .The micropore volume (V_{micro}) and external or mesopore surface area (S_{meso}) were estimated by using t-Plot method. Here, theoretically calculated thickness (t) of the adsorbed nitrogen layer on carbon black surface is used as the reference isotherm [64].

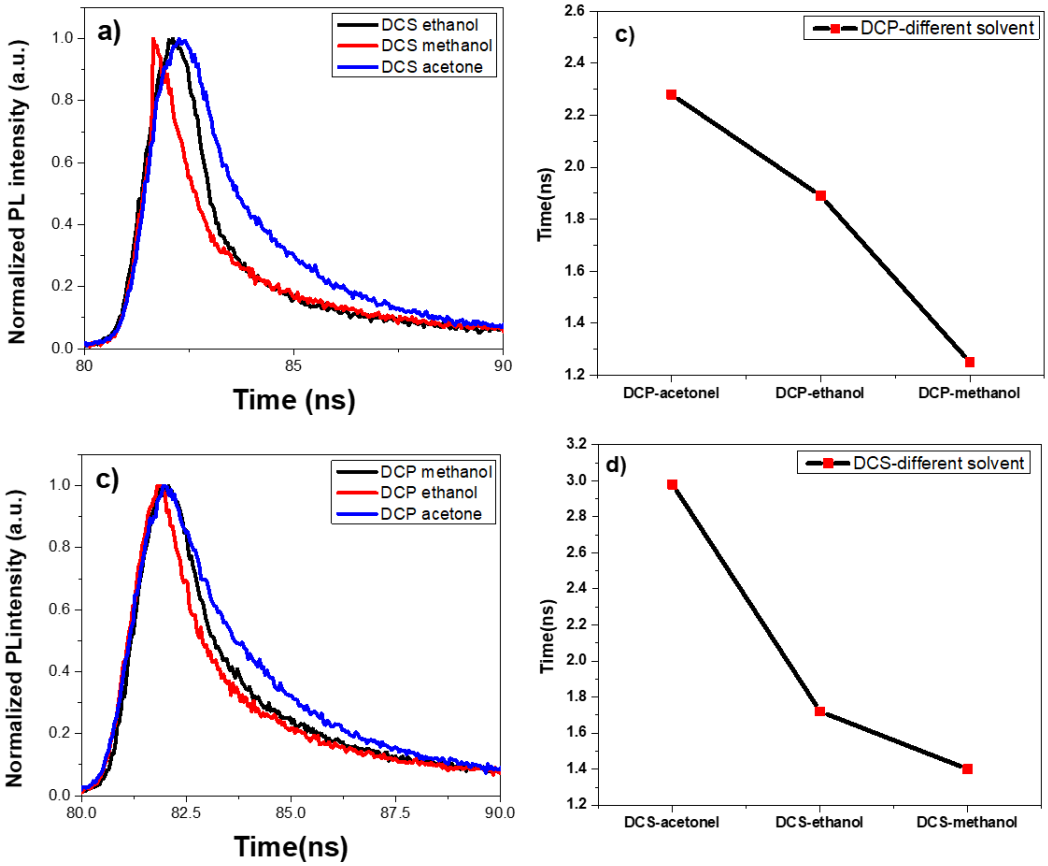

Figure 12. A representative fluorescence decay transients of (a) DCP and (c) DCS. The change in lifetime with respect to the solvents for (b) DCP and (d) DCS.

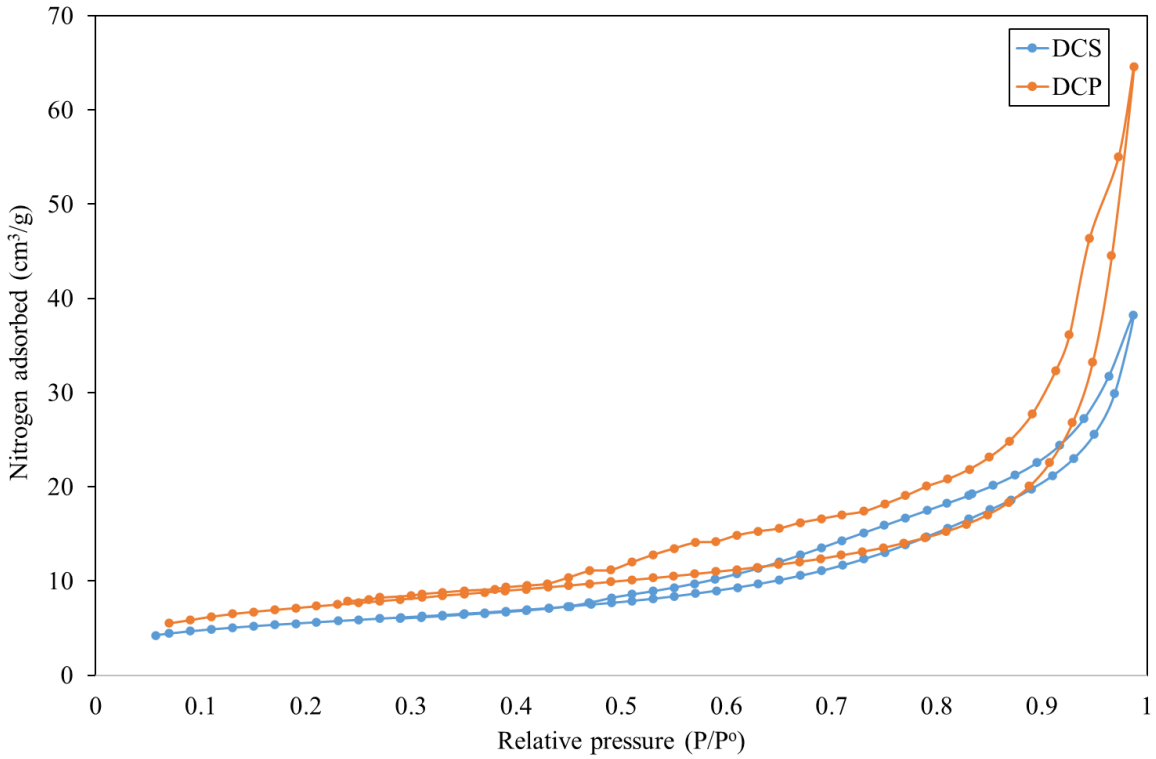

Figure 7. Nitrogen adsorption-desorption isotherms of DCP and DCS at 77 K.

The BET equation was used for the estimating total surface area (S_{BET}) which is presented in Table 3. DCP possesses a larger surface area and pore diameter than DCS. In both samples, the mesopore surface area (S_{meso}) is much larger than the micropore surface area (S_{micro}), accounting for ~ 80 % of total surface area (Table 3). V_{meso}, the volumes of mesopores, are calculated from eqn. 2, $V_{meso} = V_t - V_{mico}$ $equ.$ (2) where V_t is the total volume. V_{meso} is found to be greater than V_{micro}. Both sulfuric and phosphoric acids are dehydrating agents, but the former is a stronger oxidant than the latter. DCS possesses more carboxylic content and surface hydrophilicity than DCP. The higher carbon-oxygen content on both carbons, particularly DCS, occupies a large fraction of DCS surface, to a great extent, adsorption of the non-polar nitrogen molecule.

3.10 XPS DC

The XPS spectra of DCP and DCS are shown in Figure 8. The results after deconvolution of the spectra are given in Table 4. In both samples, there are two sub-peaks at the binding energies 284.1 eV and 532eV, which are assigned to C 1s and O 1s, respectively [65]. Figure 8(a-b) show the high-resolution XPS spectra of C 1s state. There are four sub-peaks located at 285.2 eV, 286.2 eV, 287.4 eV, and 288.3 eV which correspond to C=C, C–O, C=O, and O=C–O bonds, respectively [22, 66]. Figure 8(c-d) depicts the spectra of O 1s, showing two characteristic peaks of C=O at 533.7eV and 534.7 eV [19, 22, 67, 68]. These results are in agreement with the EDS and CHN measurements, showing a higher oxygen content in DSC than DCP.

Table 3. Surface properties of dehydrated carbons (DCS and DCP).

Carbon	BET Surface area ($\boldsymbol{SBET}$) ($\boldsymbol{m^2/g}$)	$\boldsymbol{V_t}$ ($\boldsymbol{ml/g}$)	Avr. Pore diameter D (Å)	Mesopore surface area ($\boldsymbol{Smeso}$) ($\boldsymbol{m^2/g}$)	Micropore surface area ($\boldsymbol{Smicro}$) ($\boldsymbol{m^2/g}$)	($\boldsymbol{Vmicro}$) ($\boldsymbol{ml/g}$)	($\boldsymbol{Vmeso}$) ($\boldsymbol{ml/g}$)	Apparent density ($\boldsymbol{g/cm^3}$)
DCP	25.46	0.100	156.9	20.17	5.29	0.003	0.029	0.62
DCS	19.73	0.060	119.9	15.17	4.56	0.002	0.057	0.35

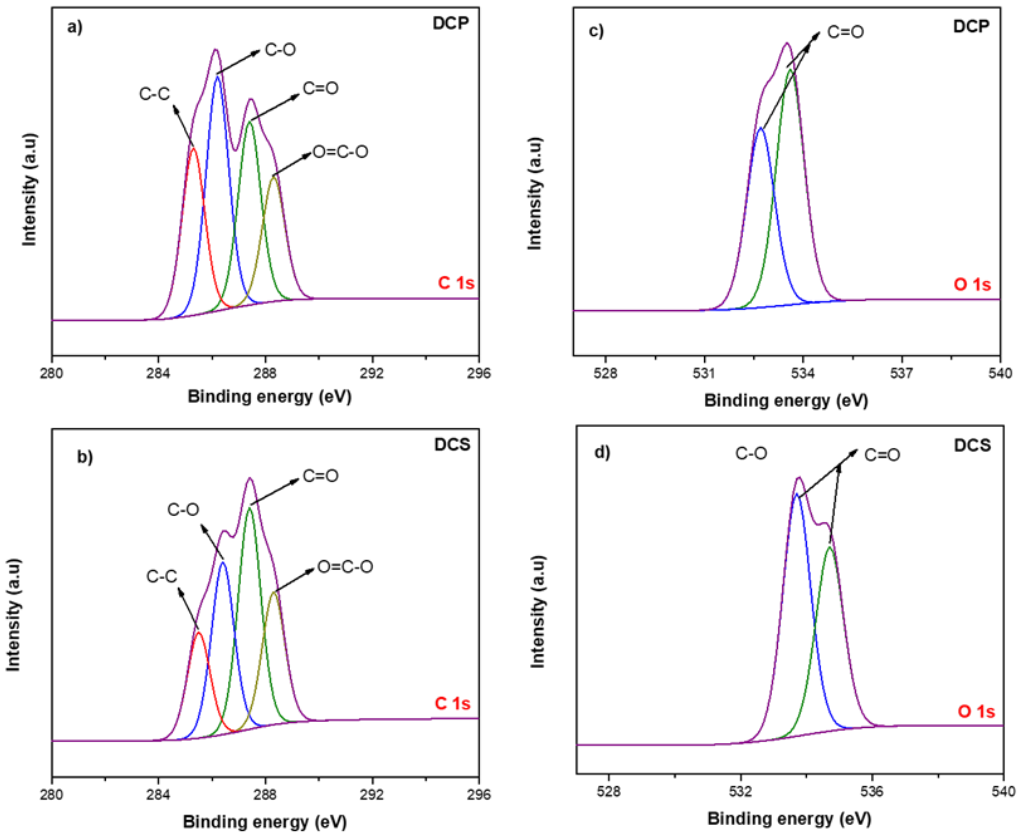

Figure 8. De-convoluted high-resolution XPS C 1s and O 1s spectra of (a-c) DCP, and (b-d) DCS.

Table 4. Estimated percentage atomic content of carbon and oxygen in DCP and DCS.

	DCP		DCS	
atom	C	O	C	O
%	87.38	12.62	79.36	20.64
FWHM (eV)	4.51	3.62	3.89	3.76
Area	4652.9	1968.5	8043.2	6127.7

3.11 Adsorption studies of methylene blue on the surface of dehydrated carbon dots

Figure 9a shows that with increasing the initial pH, MB adsorption (%) increases significantly (37%) on DCP, compared to that on DCS (43%) in the pH range 2-7. On the other hand, this variation is insignificant in the pH range 7-9. Methylene blue is a cationic dye that remains positively charged at different pH values. Thus, the variation in MB adsorption is mainly related to the pH_{zpc} values. At pH below pH_{zpc}, the dots remain neutral by carboxylic protonation. However, at values higher than pH_{zpc}, DCS and DCP dots become negatively charged. This allows more electrostatic interaction between the positively charged MB and negatively charged surfaces. However, the extent of hydrophobic interaction between MB and the dot surface is clear at low pH, particularly for DCS. Similar results were reported earlier about MB adsorption at different pH on rice hulls [69] and activated carbon [70].

The kinetics of adsorption of MB is presented in Figure 9b. Equilibrium is achieved after 12 hours in both samples and shows better performance as the temperature rises. Despite its slightly lower surface area, DCS shows better MB adsorption performance compared to DCP. As mentioned earlier, this is because DCS has a higher density of carboxylic groups that adsorb MB by electrostatic interaction. In the initial stage, MB adsorption is nearly a linear function of square root of time, which is based on the pore diffusion model [71], (see eqn. 3) $q_t = k_d\, t^{0.5}$ eqn. (3) where q_t is the adsorbed amount of MB (mg/g) at time t and k_d is the diffusion rate constant. Increasing the temperature has clearly enhanced the diffusion rate (see Table 5). MB adsorption kinetic data was analyzed by using *pseudo first-order* (*pfo*) and *second-order(pso)* kinetic models (see eqn. 4 and 5) [72].

$Log(q_e - q_t) = log(q_e) - \frac{k_1 t}{2.303}$ eqn.(4)

$\frac{t}{q_t} = \frac{1}{k_2 q_e^2} + \frac{t}{q_e}$ eqn. (5)

In the above equations, k_1 *and* k_2 represent the rate constants for *pfo* and *pso* models, respectively, while q_e is the amount of MB adsorbed at equilibrium. Herein, the initial adsorption rate is calculated from a pseudo-second-order rate constant as in eqn. 6 [73]. $h = K_2 q_e^2$ eqn. (6) *pfo* did not produce a good fit to the kinetic adsorption data (see the R^2 values in Table 5). But, the adsorption data fits very well with the *pso* model. This reflects good compliance with the *pso* model. This results suggests the possibility of sharing or exchange of electrons between the carbon surface and the MB molecules [73].

The values of k_2, k_d, and the initial rate (h) are greater for DCS than for DCP, as shown in Table 5. This is related to the higher content of the negatively charged carboxylic groups on the DCS surface. The increase in MB uptake with increasing temperature could be related to the increase in the number of active sites available on the carbon surface for adsorption as a result of the swelling of dehydrated carbon [74]. In addition, the desolvation of MB molecules decreases the thickness of the boundary wall around carbon particles; hence, the mass transfer of MB from the boundary layer to carbon increases [74, 75].

The activation energy, E_a (kJ/mol) for MB adsorption was then calculated using k_2, the pseudo-second-order rate constant in Arrhenius equation Eq.7), $ln(\frac{k'_2}{k_2}) = \frac{E_a}{R}(\frac{1}{T_1} - \frac{1}{T_2})$ Eq. (7) where R is the ideal gas constant (8.314 J/mol/K). k_2 and k'_2 are the rate constants at temperatures T_1 = 293 K, and T_2 = 313 K respectively. E_a values are lower than 40 kJ/mol, indicating that MB adsorption takes place mainly via physical diffusion-controlled processes [76]. In general, Low E_a values (5 – 40 kJ/mol) are characteristic for physisorption, while higher E_a values (40–800 kJ/mol) refer to chemisorption [77] . The estimated E_a value in this work indicates a rate-limiting process for the adsorption of MB that is dominantly physical.

The equilibrium MB adsorption data follow an L-type adsorption isotherm (Figure 9c). DCS shows higher adsorption than DCP and it increases with temperature. The MB equilibrium adsorption data was analyzed by using Langmuir and Freundlich models (eqn. 8 & 9), $C_e/q_e = 1/b.q + C_e/q$ eqn. (8)

$log\, q_e = 1/n\, log\, C_e + log\, K$ eqn.(9) where q and b are the constants of the Langmuir equation that are linked to monolayer adsorption capacity (mg/g) and relative energy of adsorption (L/mg), respectively. The parameters used in eqn. 2 such as K ($L^{1/n}\, mg^{1-1/n}\, g^{-1}$) and $1/n$ are the constants of the Freundlich equation, indicating the adsorption capacity and adsorption intensity, respectively.

MB adsorption data were found to fit well with the Langmuir model than to the Freundlich model, (see higher R^2 values in Table 6). This indicates the monolayer formation of MB on the carbon surfaces at equilibrium. Equilibrium parameters for MB adsorption at different temperatures are shown in Table 6. At pH 7, both DCS and DCP are negatively charged. Therefore, MB, which is a cationic dye, can adsorbed on DC samples through electrostatic attraction. However, due to its high carboxyl content, DCS is more negatively charged than DCP, and subsequently has a higher MB uptake, regardless of its lower surface area than DCP.

Table 5. Temperature-dependent kinetic parameters of dye adsorption.

Carbon	Temperature (oC)	Pore diffusion constant, k_d (mg/g/h0.5)	Pseudo first order model (pfo)			Pseudo second order model (pso)				Ea, (kJ/mol)
			k1 (hr-1)	qe (mg/g)	R^2	rate const. k2, (g/mg/h)	Initial adsorption rate, h, (mg/g/h)	Monolayer, qe, (mg/g)	R^2	
DCS	20	18.14	0.169	4.53	0.9840	0.0129	26.38	45.2	0.9998	21.7
	40	32.11	0.157	4.21	0.9711	0.0171	43.67	50.5	1	
DCP	20	10.64	0.154	4.30	0.9741	0.0114	16.42	38.0	0.9994	7.4
	40	19.93	0.169	4.29	0.9978	0.0125	22.27	42.2	0.9996	

Table 6. Measured equilibrium adsorption parameters at two different temperatures.

Sorbent	Sorption Temperature. (°C)	Langmuir constants		R^2	Freundlich constants		R^2
		q (mg/g)	*b* (L/mg)		*1/n*	*K*	
DCS	20	65.8	0.199	0.9998	0.416	36.0	0.8927
	40°	88.5	0.191	0.9997	0.414	53.3	0.9431
DCP	20	54.9	0.102	0.9993	0.416	26.3	0.9448
	40	69.9	0.194	0.9994	0.367	40.7	0.9322

Table 7. Temperature-dependent thermodynamics parameters of the adsorption process.

	Temperature (°C)	K_c	ΔG^o (kJ/mol)	ΔS^o(J/mol)	ΔH^o(kJ/mol)
DCS	20	110.2	-11.5	164.3	37.5
	40	294.7	-14.8	175.5	
DCP	20	78.9	-10.6	150.0	34.1
	40	192.8	-13.7	160.3	

The increased MB adsorption capacity with rising temperature is most likely related to the increased swelling of carbons and thus more access to active sites. In addition, an extent of MB and carbon desolvation decreases the thickness of boundary walls around MB and carbon particles, thus, increasing mass transfer of MB from the boundary layer to carbons [74, 75].

The equilibrium constant, $K_c = C_{Ae}/C_e$ eqn. (10) C_{Ae} and C_e are the amount of dye adsorbed on the dots (mg) per litre of solution and the equilibrium concentration of the dye solution (mg/lit), respectively.

We calculated the thermodynamic parameters from the changes observed in K_c at temperatures 20 and 40 °C. K_c is obtained from the initial, linear part of the adsorption isotherm. Eqn. 11 shows the relation between K_c and change in Gibbs free energy ($\Delta G°$) of the adsorption process [78].

$\Delta G^o = -RTlnK_c$ eqn. (11)

The entropy change, ΔS^o, is positive, which suggests that the degree of randomness of adsorption is increasing [80]; similar results were reported for MB adsorption on activated carbon [11].

The percentage of MB removed from the solution is calculated as follows:

$$Removal(\%) = \frac{(C_o - C_t)}{C_o} \times 100$$

Eq. (14). Where C_o is the initial MB concentration and C_t (mg L^{-1}) is the concentration at time t [81].

The adsorption of MB at different carbon masses is presented in Figure 9d. The percentage of MB removal increases with an increase in carbon mass. Correspondingly, the adsorption capacity is found to decrease (mg/g). The addition of more dots increases the active sites for MB adsorption; thus, the percentage removal increases. MB adsorption capacity (mg/g) decreases as the carbon mass increases. This can be explained in the following way. The concentration of MB molecules will be relatively high at low amounts of carbon. This leads to high adsorption on the limited active sites on the sorbent surface. As the amount of carbon dots increases, more active sites are available for MB molecules and, therefore, not fully occupied. Besides, particle interaction and aggregation of dots are possible. Consequently, the vacant active sites for adsorption reduce and the MB adsorption capacity (mg/g) decreases [82].

From Van't Hoff equation (Eqn. 12) we calculated the enthalpy (ΔH^o) [78].

$$\ln\left(\frac{k_{c2}}{k_{c1}}\right) = \frac{\Delta H^o}{R}\left(\frac{1}{T_1} - \frac{1}{T_2}\right) \text{ eqn. (12)}$$

Here, k_{c1} and k_{c2} are the equilibrium constants at two temperatures, T_1 and T_2, respectively.

The entropy change, ΔS^o can be calculated from the following equation.

$\Delta G^\circ = \Delta H^\circ - T\Delta S^\circ$ eqn. (13).

As presented in Table 7, the increasing K_c with temperature and the positive values of ΔH^o represent an endothermic adsorption process [74]. ΔH^o less than 40 kJ/mol, indicates physisorption. At the same time, the negative ΔG^o is because of the spontaneous adsorption processes at both temperatures. In addition, the ΔG^o values further decrease with increasing temperature, indicating enhanced MB adsorption [79].

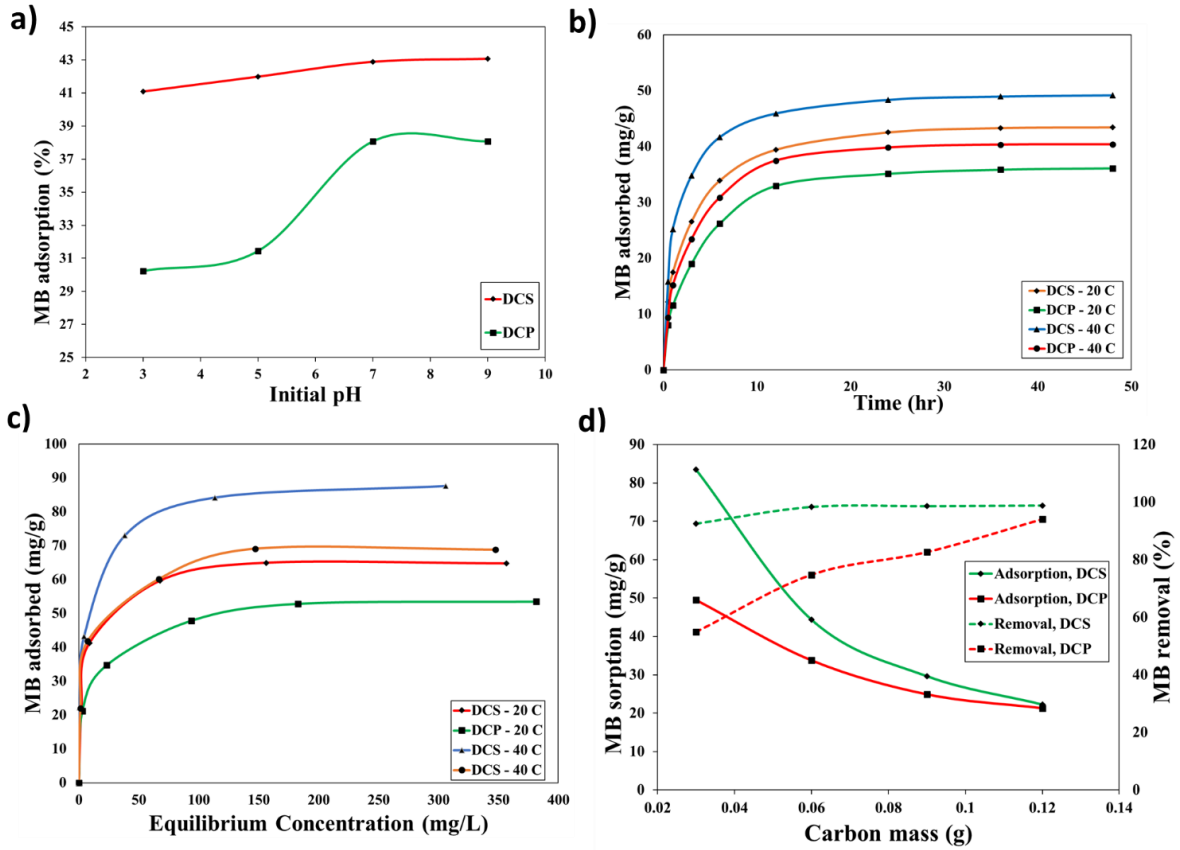

Figure 9. **a)** Effect of initial pH on MB sorption at 20 °C. **b)** Kinetics of MB sorption on the different sorbents at 25 °C. **c)** MB adsorption isotherms on dehydrated carbons at 20 and 40 °C. **d)** Adsorption of MB at different Carbon masses.

4. Conclusion

Dehydrated carbon dots (DC) were prepared via the dehydrative effect of H_3PO_4 (DCP) or H_2SO_4 (DCS) on an agricultural green waste (mandarin peels) as a precursor material. The average particle size distribution was about 2.63±0.2 nm for DCS and 3.34 ± 0.1 nm for DCP. The average lattice spacing was 0.29 ± 0.01 nm for DCP and 0.27 ± 0.01 nm for DCS. These values are similar to the spacings of graphite (002) facets (0.34 nm). DCP has a point of zero charge (pHzpc) of 3.62 ± 0.6, while the DCS sample had a pHzpc of 3.26 ± 0.4, indicating a higher surface acidity than DCP. This observation could be linked to an increased oxidation power when sulfuric acid is used instead of phosphoric acid. The results of Boehm titration show that the proportion of carbonyl group density in the DCP-DCS samples is around 1.18 meq/g in DCP compared with DCS, which is around 0.52 meq/g. DCP possesses a higher surface area (S_{BET}) and a larger pore diameter than DCS. Functional groups such as carbonyl, phenol, lactone and carboxylic were detected on DCS and DCP. The pseudo-second model suggests the possibility of electron exchange between the dot and MB dye molecule. Moreover, the increased MB adsorption capability as the temperature rises is most likely due to increased carbon swelling and more access to active sites. The values of ΔH^o are positive, indicating that MB adsorption is endothermic. Since the observed values of ΔH^o are less than 40 kJ/mol, the adsorption mechanism could be physisorption. However, DCS shows a higher monolayer capacity for MB than DCP due to its high carboxyl content, which adsorbs MB by electrostatic interaction. DCS is more negatively charged than DCP and shows a higher MB uptake, regardless of its lower surface area than DCP. In general, DCS shows better MB adsorption performance compared to DCP. The deconvoluted PL emission peaks are attributed mainly to carboxylic, carbonyl groups, and the sp^2 clusters attached to the surface of the dots. Solvent polarity has a vital role in the emission characteristics of fluorescent materials. The PL peak shows a hypsochromic shift with the increasing solvent polarity. This shift is mainly for the emission peak associated with the carbonyl group. The carbonyl group is polar, and the strong interaction with polar molecules is known to reduce the energy gap. In the decay transients there are fast and slow components. It can be noticed that the average lifetime depends on the polarity of the solvent. In high-polarity solvents such as methanol, the average lifetime is 1.4 ns (DCS) and 1.27 ns (DCP). Whereas in non-polar solvents like acetone, the average lifetime is around 2.98 ns (DCS) and 2.27 ns (DCP). This could be because of the increased non-radiative transitions due to the strong vibrational coupling of the dots with the polar solvent molecules.

Conflict of interest

The authors declare no conflict of interest.

Acknowledgement

We gratefully acknowledge the financial support from Sultan Qaboos University within the framework of research Internal Grant [IG/SCI/PHYS/18/05] and His Majesty's Trust Fund for Strategic Research (SR/SCI/CHEM/18/01). Further, we thank the Central Analytical and Applied Research Unit at Sultan Qaboos University for the XRD measurements.

References

1. Niu, T., Zhou, J., Zhang, C. and Li, S. Fast removal of methylene blue from aqueous solution using coal-based activated carbon. RSC Advances, 2018, **8(47)**, 26978-26986.
2. Dulo, B., Phan, K., Githaiga, J., Raes, K. and De Meester, S. Natural Quinone Dyes: A Review on Structure, Extraction Techniques, Analysis and Application Potential. Waste and Biomass Valorization, 2021.
3. Lellis, B., Fávaro-Polonio, C.Z., Pamphile, J.A. and Polonio, J.C. Effects of textile dyes on health and the environment and bioremediation potential of living organisms. Biotechnology Research and Innovation, 2019, **3(2)**, 275-290.
4. Collivignarelli, M.C., Abba, A., Carnevale Miino, M. and Damiani, S. Treatments for color removal from wastewater: State of the art. *Journal of Environmental Management*, 2019. **236**, 727-745.
5. Mohd Azmy, H.A., Razuki, N.A., Aziz, A.W., Abdul Satar, N.S. and Mohd Kaus, N.H. Visible Light Photocatalytic Activity of BiFeO3 Nanoparticles for Degradation of Methylene Blue. *Journal of Physical Science*, 2017, **28(2)**, 85-103.
6. Carmen, Z. and Daniel, S. Textile Organic Dyes – Characteristics, Polluting Effects and Separation/Elimination Procedures from Industrial Effluents – A Critical Overview. 2012.
7. El-Shafey el, S.I. and Al-Kindy, S.M. Removal of Cu2+ and Ag+ from aqueous solution on a chemically-carbonized sorbent from date palm leaflets. *Environmental Technology*, 2013, **34(1-4)**, 395-406.
8. El-Shafey, E.I., Ali, S.N.F., Al-Busafi, S. and Al-Lawati, H.A.J. Preparation and characterization of surface functionalized activated carbons from date palm leaflets and application for methylene blue removal. *Journal of Environmental Chemical Engineering*, 2016, **4(3),** 2713-2724.
9. Jiao, Y., Sun, H., Jia, Y., Liu, Y., Gao, Y., Xian, M., Shuang, S. and Dong, C. Functionalized fluorescent carbon nanoparticles for sensitively targeted of folate-receptor-positive cancer cells. *Microchemical Journal*, 2019, **146**, 464-470.
10. Jun Wang, F.-A.W., Meng Wang, Ning Qiu, Yao Liang, Shui-Qin Fang. and Xing Jiang, Preparation of activated carbon from a renewable agricultural residue of pruning mulberry shoot. *African Journal of Biotechnology* 2019, **9**, 2762-2767.
11. Kuang, Y., Zhang, X. and Zhou, S. Adsorption of Methylene Blue in Water onto Activated Carbon by Surfactant Modification. Water, 2020, **12(2)**, 587.
12. El-Said I. El-Shafey, S.N.F.A., Al-Lawati, Haider and Saleh, N. Al-Busafi. Preparation and Characterization of Acidic, Basic and Hydrophobic Dehydrated Carbons and their Capability for Methylene Blue Adsorption. *SQU Journal for Science*, 2019, **24(1)**, 23-35.
13. El-Shafey, E.-S.I., Al-Lawati, H.A.J. and Al-Hussaini, A.Y. Adsorption of fexofenadine and diphenhydramine on dehydrated and activated carbons from date palm leaflets. Chemistry and Ecology, 2014, **30(8)**, 765-783.
14. Ghosal, K. and A. Ghosh, Carbon dots: The next generation platform for biomedical applications. Mater Sci Eng C Mater Biol Appl, 2019, **96**, 887-903.
15. Liu, Q., Sun, J., Gao, K., Chen, N., Sun, X., Ti, D., Bai, C., Cui, R. and Qu, L. Graphene quantum dots for energy storage and conversion: from fabrication to applications. Materials Chemistry Frontiers, 2020, **4(2)**, 421-436.
16. Sharma, A. and Das, J. Small molecules derived carbon dots: synthesis and applications in sensing, catalysis, imaging, and biomedicine. *Journal of Nanobiotechnology*, 2019, **17(1)**, 92.
17. El-Shabasy, R.M., Farouk Elsadek, M., Mohamed Ahmed, B., Fawzy Farahat, M., Mosleh, K.N. and Taher, M.M. Recent Developments in Carbon Quantum Dots: Properties, Fabrication Techniques, and Bio-Applications. Processes, 2021, **9(2)**, 388.
18. Li, H., Ming, H., Liu, Y., Yu, H., He, X., Huang, H., Pan, K., Kang, Z. and Lee, S.-T. Fluorescent carbon nanoparticles: electrochemical synthesis and their pH sensitive photoluminescence properties. *New Journal of Chemistry*, 2011, **35(11)**, 2666.
19. Al Farsi, B., Sumesh Sofin, R.G., El-Shafey, E.-S.I., Issac, A., Al Marzouqi, F., Al Mashaikhi, S., Zar Myint, M.T. and Abou-Zied, O.K. Controlling the emissive pathways of carbon nanoparticles by selective surface functionalization. Applied Surface Science, 2021, **566**, 150618.
20. Valério Filho, A., Xavaré Kulman, R., Vaz Tholozan, L., Felkl de Almeida, A.R. and Silveira da Rosa, G. Preparation and Characterization of Activated Carbon Obtained from Water Treatment Plant Sludge for Removal of Cationic Dye from Wastewater. Processes, 2020, **8(12)**, 1549.
21. Li, Y., Shu, H., Niu, X. and Wang, J. Electronic and Optical Properties of Edge-Functionalized Graphene Quantum Dots and the Underlying Mechanism. *The Journal of Physical Chemistry* C, 2015, **119(44)**, 24950-24957.
22. Al Farsi, B., Sofin, R.G.S., Al Shidhani, H. , El-Shafey, E.-S.I., Al-Hosni, A.S., Al Marzouqi, F., Issac, A., Al Nabhani, A. and Abou-Zied, O.K. The effect of microwave power level and post-synthesis annealing treatment on oxygen-based functional groups present on

carbon quantum dots. *Journal of Luminescence*, 2022, **252**,119326.
23. Sofin, R.G.S.A.I., Al-Naabi, M.R.S., Zar Myint, M.T., Htet Kyaw, H. and Osama.K.Abou-Zied, Emission characteristics of carbon films in comparison with solvatochromic effects of carbon nanoparticles. Spectrochimica Acta Part A: Molecular and Biomolecular Spectroscopy, 2021, 1386-1425.
24. Li, H., Sun, Z., Zhang, L., Tian, Y., Cui, G. and Yan, S. A cost-effective porous carbon derived from pomelo peel for the removal of methyl orange from aqueous solution. Colloids and Surfaces A: Physicochemical and Engineering Aspects, 2016, **489**, 191-199.
25. Sunarno, I., Rachmat, D., Agustin, A.D., Risanti, D.D., Pulung Sasmito, A. and Peng Hong, L. Purification of Biodiesel Using Activated Carbon Produced from Cocoa Pod Husk. E3S Web of Conferences, 2018, **42**, 01012.
26. Zhao, Y., Zhang, Y., Liu, X., Kong, H., Wang, Y.m, Qin, G., Cao, P., Song, X., Yan, X., Wang, Q. and Qu, H. Novel carbon quantum dots from egg yolk oil and their haemostatic effects. Sci Rep, 2017, **7(1)**,4452.
27. Sahu, S., Behera, B., Maiti, T.K. and Mohapatra, S. Simple one-step synthesis of highly luminescent carbon dots from orange juice: application as excellent bio-imaging agents. Chem Commun (Camb), 2012, **48(70)**, 8835-7.
28. Boehm, H.P. Chemical Identification of Surface Groups. 1966, **16**, 179-274.Rivin, D., Use of Lithium Aluminum Hydride in the Study of Surface Chemistry of Carbon Black. Rubber Chemistry and Technology, 1963, **36(3)**,729-739.
29. Moreno-Castilla, C., M.A.F.-G., Joly, J.P., Bautista-Toledo, I., Carrasco- Marin, F. and Rivera-Utrilla, J. Activated carbon surface modifications by nitric acid, hydrogen peroxide, and ammonium peroxydisulfate treatments, Langmuir 11, 1995, 4386-4392.
30. Leyvaramos, R., Bernaljacome, L. and Acostarodriguez, I. Adsorption of cadmium(II) from aqueous solution on natural and oxidized corncob. Separation and Purification Technology, 2005, **45(1)**, 41-49.
31. Moreno-Castilla, M.V.L.-R.C. and Carrasco-Marın, F. Changes in surface chemistry of activated carbons by wet oxidation. Carbon, 2000, **38**,1995-2001.
32. Qiu, X., Wang, L., Zhu, H., Guan, Y. and Zhang, Q. Lightweight and efficient microwave absorbing materials based on walnut shell-derived nano-porous carbon. Nanoscale, 2017, **9(22)**, 7408-7418.
33. Wong, K.T., Yoon, Y. and Jang, M. Enhanced Recyclable Magnetized Palm Shell Waste-Based Powdered Activated Carbon for the Removal of Ibuprofen: Insights for Kinetics and Mechanisms. PLoS One, 2015, **10(10)**, e0141013.
34. Liu, X.-Y., Huang, M., Ma, H.-L., Zhang, Z.-Q., Gao, J.-M., Zhu, Y.-L., Han, X.-J. and Guo, X.-Y. Preparation of a Carbon-Based Solid Acid Catalyst by Sulfonating Activated Carbon in a Chemical Reduction Process. Molecules, 2010, **15(10)**, 7188-7196.
35. Jurkiewicz, K., Pawlyta, M. and Burian, A. Structure of Carbon Materials Explored by Local Transmission Electron Microscopy and Global Powder Diffraction Probes. C, 2018, **4(4)**, 68.
36. Khalid, M. Omer, D.I.T. and Aso Q. Hassan. Solvothermal synthesis of phosphorus and nitrogen doped carbon quantum dots as a fluorescent probe for iron(III). Springer Nature, 2018, **185(10)**, 1-8.
37. Sasaki, Y., Takeda, A., Kiyoto, S. Ohshio, H. Akasaka, M. and Nakano, H. Saitoh. Evaluation of etching on amorphous carbon films in nitric acid. Diamond and Related Materials, 2012, **24**, 104-106.
38. Lou, Z., Huang, H., Li, M., Shang, T. and Chen. C. Controlled Synthesis of Carbon Nanoparticles in a Supercritical Carbon Disulfide System. Materials (Basel), 2013, **7(1)**, 97-105.
39. Nawal Ahmad Alarfaj , M.F.E.-T.a.H.F.O., CA 19-9 Pancreatic Tumor Marker Fluorescence Immunosensing Detection via Immobilized Carbon Quantum Dots Conjugated Gold Nanocomposite. Molecular sciences, 2018, 16.
40. Akansha Dager, T.U., Toru Maekawa and Masaru Tachibana, Synthesis and characterization of Mono-disperse Carbon Quantum Dots from Fennel Seeds: Photoluminescence analysis using Machine Learning Scientific Reports, 2019, 12.
41. Shidhani, H.A. Studies on Doped and Annealed Tungsten Trioxide (wo3) Particles. Sultan Qaboos University 2022.
42. El-Shafey, E.S.I., Immobilization of Hg (II) to Hg (0) on Reducing Dehydrated Carbons. *Journal of Medical and Bioengineering*, 2014, 292-296.
43. Yin, C., Aroua, M. and Daud, W. Review of modifications of activated carbon for enhancing contaminant uptakes from aqueous solutions. Separation and Purification Technology, 2007, **52(3)**, 403-415.
44. Yang, X., Shi, G., Wu, C., Sun, H. Theoretical determination of zeta potential for the variable charge soil considering the pH variation based on the Stern-Gouy double-layer model. Environ Sci Pollut Res Int, 2023, **30(9)**, 24742-24750.
45. Chungsying Lu, H.C. and Chunti Liu, Removal of Zinc(II) from Aqueous Solution by Purified Carbon Nanotubes: Kinetics and Equilibrium Studies. Ind. Eng. Chem. Res, 2006, **45**, 2850-2855.
46. Harry, I.D., Saha, B. and Cumming, I.W. Effect of electrochemical oxidation of activated carbon fiber on competitive and noncompetitive sorption of trace toxic metal ions from aqueous solution. *Journal of Colloid Interface Science*, 2006, **304(1)**, 9-20.
47. Sunday, E. and Elaigwu, G.M.G. Chemical structural and energy properties of hydrochars from microwave-assisted hydrothermal carbonization of glucose. Springerlink, 2016(7), 449-456.
48. Wiedner, K., Naisse, C., Rumpel, C., Pozzi, A., Wieczorek, P., Glaser, B. Chemical modification of biomass residues during hydrothermal carbonization – What makes the difference, temperature or feedstock? Organic Geochemistry, 2013, **54**, 91-100.

49. Pandey, S., Mewada, A., Thakur, M., Tank, A., Sharon, M. Cysteamine hydrochloride protected carbon dots as a vehicle for the efficient release of the anti-schizophrenic drug haloperidol. *RSC Advances*, 2013, **3(48)**, 26290.
50. Wang, D., Wang, Z., Zhan, Q., Pu, Y., Wang, J.-X., Foster, N.R. and Dai, L. Facile and Scalable Preparation of Fluorescent Carbon Dots for Multifunctional Applications. Engineering, 2017, **3(3)**, p. 402-408.
51. Liu, Q.Q., Zhang, S.H., Yang, J. and Yue, Kf. A water-stable La-MOF with high fluorescence sensing and supercapacitive performances. Analyst, 2019. **144(15)**, 4534-4544.
52. Emam, A.N., Loutfy, S.A., Mostafa, A.A., Awad, H., Mohamed, M.B. Cyto-toxicity, biocompatibility and cellular response of carbon dots–plasmonic based nano-hybrids for bioimaging. RSC Advances, 2017, **7(38)**, 23502-23514.
53. Abdullah Issa, M., Z, Z.A., Sobri, S., Rashid, S., Adzir Mahdi, M., Azowa Ibrahim, N. and M, Y.P. Facile Synthesis of Nitrogen-Doped Carbon Dots from Lignocellulosic Waste. Nanomaterials (Basel), 2019, **9(10)**.
54. Pal, T., Mohiyuddin, S. and Packirisamy, G. Facile and Green Synthesis of Multicolor Fluorescence Carbon Dots from Curcumin: In Vitro and in Vivo Bioimaging and Other Applications. ACS Omega, 2018, **3(1)**, 831-843.
55. Pramanik, A., Biswas, S. and Kumbhakar, P. Solvatochromism in highly luminescent environmental friendly carbon quantum dots for sensing applications: Conversion of bio-waste into bio-asset. Spectrochim Acta A Mol Biomol Spectrosc, 2018, **191**, 498-512.
56. Pan, D., Zhang, J., Li, Z., Wu, C., Yan, X. and Wu, M. Observation of pH-, solvent-, spin-, and excitation-dependent blue photoluminescence from carbon nanoparticles. Chem Commun (Camb), 2010, **46(21)**, 3681-3.
57. Lee, H.J., Jana, J., Thi Ngo, Y.-L., Wang, L.L., Chung, J.S. and Hur, S.H. The effect of solvent polarity on emission properties of carbon dots and their uses in colorimetric sensors for water and humidity. Materials Research Bulletin, 2019, **119**, 110564.
58. Fang, Q., Dong, Y., Chen, Y., Lu, C.-H., Chi, Y., Yang, H.-H., Yu, T. Luminescence origin of carbon based dots obtained from citric acid and amino group-containing molecules. Carbon, 2017, **118**, 319-326.
59. Yu, J., Liu, C., Yuan, K., Lu, Z., Cheng, Y., Li, L., Zhang, X., Jin, P., Meng, F., Liu, H. Luminescence Mechanism of Carbon Dots by Tailoring Functional Groups for Sensing Fe(3+) Ions. Nanomaterials (Basel), 2018, **8(4)**.
60. Du, J., Wang, H., Wang, L., Zhu, S., Song, Y., Yang, B. and Sun, H. Insight into the effect of functional groups on visible-fluorescence emissions of graphene quantum dots. *Journal of Materials Chemistry* C, 2016, **4(11)**, 2235-2242.
61. Thommes, M., Physical adsorption characterization of nanoporous materials. Chem-Ing-Tech., 2010, 1059-1073.
62. S. Lowell, J.E.S., M.A. Thomas, M. Thommes, characterization of porous solids and powders: surface area, pore size and density. Springer Science and Business Media, 2012, **16**.
63. Standard test method for carbon black- total and external surface area by nitrogen adsorption. ASTM standards, 2012, D-6556-01.
64. Awati, A., Maimaiti, H., Xu, B. and Wang, S. A comparative study on the preparation methods and properties of coal-based fluorescent carbon nanoparticles. Surface and Interface Analysis, 2019, **52(3)**, 98-109.
65. Roy, S., Das, T., Ming, Y., Chen, X. , Yue, C.Y. and Hu. X. Specific functionalization and polymer grafting on multiwalled carbon nanotubes to fabricate advanced nylon 12 composites. *Journal of Materials Chemistry A*, 2014, **2(11)**, 3961.
66. Rojas, J.V., Toro-Gonzalez, M., Molina-Higgins, M.C. and Castano., C.E. Facile radiolytic synthesis of ruthenium nanoparticles on graphene oxide and carbon nanotubes. Materials Science and Engineering: B, 2016, **205**, 28-35.
67. Al Ghafry, S.S.A., Al Shidhani, H., Al Farsi, B., Sofin, R.G.S., Al-Hosni, A.S., Alsharji, Z., Al-Sabahi, J. and Al-Abri, M.Z. The photocatalytic degradation of phenol under solar irradiation using microwave-assisted Ag-doped ZnO nanostructures. Optical Materials, 2023, **135**, 113272.
68. El-maghraby, H.A.E.D.A. Removal of a basic dye from aqueous solution by adsorption using rice hulls. *Global NEST Journal*, 2011, **13(1)**, 90-98.
69. Vimalkumar, J.T.A., Rajasekaran, K., Raja, C. and Flora, M.N. Preparation of activated carbon from mixed peels of fruits with chemical activation (K_2CO_3) application in adsorptive removal of methylene blue from aqueous solution. *International Journal of Environment and Waste Management*, 2018, **22(1-4)**, 260-271.
70. Weber, W.J. and Morris, J.C. , Kinetics of adsorption on carbon from solution. the Sanitary Engineering Division, 1963, **89(2)**, 31-60.
71. Feng, P.S.a.X. Kinetic Models on Chromium (VI) Adsorption onto Carbonized Oil Palm Kernel with Potassium Hydroxide Activation. *International Journal of Advances in Chemical Engineering and Biological Sciences*, 2016, **3(1)**.
72. Y.S. Ho, G.M., Sorption of dye from aqueous solution by peat Chemical Engineering Journal 1998, **70**, 115-124.
73. El-Shafey, E.S.I., Al-Lawati, H.A., Al-Saidi, W.S., Adsorption of lisinopril and chlorpheniramine from aqueous solution on dehydrated and activated carbons. Carbon letters, 2016, **19(1)**, 12-22.
74. Meena, A.K., Kadirvelu, K., Mishraa, G.K., Rajagopal, C., Nagar, P.N. Adsorption of Pb(II) and Cd(II) metal ions from aqueous solutions by mustard husk. *Journal of Hazardous Material*, 2008. **150(3)**, 619-25.
75. Liu, C. and Huang, P.M. Kinetics of lead adsorption by iron oxides formed under the influence of citrate. Geochimica et Cosmochimica Acta, 2003, **67(5)**, 1045-1054.

76. Figueiredo, J.L., Pereira, M.F.R., Feritas, M.M.A. Freitas, Orfao, J.J.M. Modification of the surface chemistry of activated carbons Carbon, 1999, **73**, 1379-1389.
77. Hasan Uslu, a.I.I., Adsorption Equilibria of L-(+)-Tartaric Acid onto Alumina *Journal of Chemical Engineering Data*, 2009, **54**, 1997-2001.
78. Fathy, N.A., Sayed Ahmed, S.A. and Abo El-enin, R.M.M. Effect of Activation Temperature on Textural and Adsorptive Properties for Activated Carbon Derived from Local Reed Biomass: Removal of p-Nitrophenol. Environmental Research, *Engineering and Management*, 2012, **59(1)**.
79. Fan, S., Wang Y., Wang, Z., Tang, J., Tang, J., Li, X. Removal of methylene blue from aqueous solution by sewage sludge-derived biochar: Adsorption kinetics, equilibrium, thermodynamics and mechanism. *Journal of Environmental Chemical Engineering*, 2017, **5(1)**, 601-611.
80. Geçgel, Ü., G. Özcan. and G.Ç. Gürpınar, Removal of Methylene Blue from Aqueous Solution by Activated Carbon Prepared from Pea Shells (Pisum sativum). *Journal of Chemistry*, 2013, **2013**, 1-9.
81. Tang, C., Shu, Y., Zhang, R., Li, X., Song, J., Li, B., Zhang, Y. and Ou, D. Comparison of the removal and adsorption mechanisms of cadmium and lead from aqueous solution by activated carbons prepared from Typha angustifolia and Salix matsudana. *RSC Advances*, 2017, **7(26)**, 16092-16103.